

View Article Online
View Journal

# Journal of Materials Chemistry A

Materials for energy and sustainability

#### Accepted Manuscript

This article can be cited before page numbers have been issued, to do this please use: R. Oppong, S. A. Southern, C. Martin, I. Freebairn, A. Sarkar, Y. Abusa, G. Viswanathan, F. Perras, S. W. Martin and K. Kovnir, *J. Mater. Chem. A*, 2025, DOI: 10.1039/D5TA06486D.



This is an Accepted Manuscript, which has been through the Royal Society of Chemistry peer review process and has been accepted for publication.

Accepted Manuscripts are published online shortly after acceptance, before technical editing, formatting and proof reading. Using this free service, authors can make their results available to the community, in citable form, before we publish the edited article. We will replace this Accepted Manuscript with the edited and formatted Advance Article as soon as it is available.

You can find more information about Accepted Manuscripts in the <u>Information for Authors</u>.

Please note that technical editing may introduce minor changes to the text and/or graphics, which may alter content. The journal's standard <u>Terms & Conditions</u> and the <u>Ethical guidelines</u> still apply. In no event shall the Royal Society of Chemistry be held responsible for any errors or omissions in this Accepted Manuscript or any consequences arising from the use of any information it contains.



### Come for predictions, stay for complexity: Synthesis and experimental probing of ionic conductivity in Li<sub>9</sub>B<sub>19</sub>S<sub>33</sub>

Richeal A. Oppong<sup>1,2</sup>, Scott A. Southern<sup>3</sup>, Chris Martin<sup>2</sup>, Isabella Freebairn<sup>1</sup>, Arka Sarkar<sup>1,4</sup>, Yao Abusa<sup>1</sup>, Gayatri Viswanathan<sup>1,4</sup>, Frédéric A. Perras<sup>1,3</sup>, Steve W. Martin<sup>2,\*</sup>, Kirill Kovnir<sup>1,4,\*</sup>

- <sup>1</sup> Department of Chemistry, Iowa State University, Ames, Iowa 50011, USA
- <sup>2</sup> Department of Materials Science and Engineering, Iowa State University, Ames, Iowa 50011, USA
- <sup>3</sup> Chemical and Biological Sciences Division, Ames National Laboratory, Ames, Iowa 50011, USA
- <sup>4</sup> Materials Sciences and Engineering Division, Ames National Laboratory, Ames, Iowa 50011, USA

Corresponding authors: Steve W. Martin <a href="mailto:swmartin@iastate.edu">swmartin@iastate.edu</a>, Kirill Kovnir

kovnir@iastate.edu

Article. Published on 11 nóvember 2025. Downloaded on

#### **ABSTRACT**

Lithium thioborates, despite their potential cost-effectiveness and low density, have received considerably less attention as solid electrolytes compared to their thiophosphate counterparts. A primary obstacle to their widespread investigation has been the inherent challenge in synthesizing single-phase materials. Computational studies have predicted several lithium thioborate phases exhibiting high ionic conductivity, with Li<sub>9</sub>B<sub>19</sub>S<sub>33</sub> notably predicted to reach 80 mS/cm. However, experimental validation of these theoretical predictions remains absent. This work addresses this gap by detailing a successful synthesis of the previously elusive Li<sub>9</sub>B<sub>19</sub>S<sub>33</sub> phase, facilitated by in situ temperature dependent powder X-ray diffraction (PXRD). Our findings reveal the peritectic nature of this phase formation, necessitating an excess of boron sulfide in the reaction mixture. We further present a comprehensive structural characterization of Li<sub>9</sub>B<sub>19</sub>S<sub>33</sub> utilizing spectroscopic techniques like NMR, FT-IR, and diffuse reflectance and report on ionic conductivity of Li<sub>9</sub>B<sub>19</sub>S<sub>33</sub> samples. Solid-state <sup>6</sup>Li NMR line narrowing experiments revealed an ion mobility activation energy of 0.26 eV whereas activation energies derived from impedance spectroscopy measurements were significantly higher, resulting in lower than theoretically predicted ionic conductivity. Herein the successful synthesis of the Li<sub>9</sub>B<sub>19</sub>S<sub>33</sub> phase offers a route to obtaining other challenging single-phase thioborates that can be used for all-solid-state batteries.

#### INTRODUCTION

Central to the functionality of electric vehicles (EVs) are their batteries. Currently, the most widely used lithium-ion batteries utilize organic liquid electrolytes (OLEs), that involve inherent risks owing to their flammability and the potential for spontaneous combustion. To address this issue and achieve higher energy densities, all-solid-state batteries (ASSBs) are being developed.<sup>1</sup> Solid electrolytes (SEs) are the critical component of ASSBs and can be made from materials such as sulfides, oxides, polymers, halides, or hydrides.<sup>2–10</sup> For a solid electrolyte to be high performing, it must exhibit high ionic conductivity, low electrical conductivity, and a wide electrochemical stability window.<sup>11,12</sup>

The high polarizability of S<sup>2-</sup> ions tends to facilitate the mobility of Li<sup>+</sup> ions. <sup>13,14</sup> Additionally, sulfur's large ionic radius can create bigger conduction channels and/or larger accessible empty volumes for Li<sup>+</sup> ion diffusion enabling sulfide SEs to have (typically) significantly higher ionic conductivities than a corresponding oxide SE. In particular, lithium thiophosphate-based SEs have shown promise in this field owing to their high ionic conductivity, mechanical ductility, and low mass density. <sup>15–18</sup> Some noteworthy examples are Li<sub>10</sub>GeP<sub>2</sub>S<sub>12</sub> and Li<sub>9.54</sub>Si<sub>1.74</sub>P<sub>1.44</sub>S<sub>11.7</sub>Cl<sub>0.3</sub> that have room temperature ionic conductivities of 12 mS/cm and 25 mS/cm, respectively. <sup>9,19</sup> These conductivities are comparable to, or even surpass, traditional OLEs. However, these thiophosphates have a narrow electrochemical stability window<sup>20</sup> which limits their stability in contact with low

Article. Published on 11 nóvember 2025. Downloaded on 14.11.2025 15:27:57

voltage Li metal anodes and high voltage transition metal cathodes. Additionally, the use of germanium in Li<sub>10</sub>GeP<sub>2</sub>S<sub>12</sub> makes it costly, emphasizing the need for more affordable sulfide electrolyte alternatives.

Utilizing Density Functional Theory (DFT) calculations coupled with grand potential phase analysis, four single-crystal phases of lithium thioborate, Li<sub>3</sub>BS<sub>3</sub>, Li<sub>2</sub>B<sub>2</sub>S<sub>5</sub>, Li<sub>5</sub>B<sub>7</sub>S<sub>13</sub>, and Li<sub>9</sub>B<sub>19</sub>S<sub>33</sub> have been predicted to exhibit high ionic conductivity and a wider electrochemical stability window.<sup>21</sup> Despite these theoretical findings, the experimental realization of phase-pure material for any of these phases has proven difficult, often resulting in multiphase mixtures. This is because lithium thioborates generally require higher temperatures and longer annealing times when compared with thiophosphates. Syntheses of thioborates is typically done inside sealed silica glass ampoules which are known to react vigorously with  $B_2S_3$  at temperatures above 450 °C.<sup>22,23</sup> For these reasons, it has been challenging to obtain a single phase of thioborates materials.

Kaup et al. reported the synthesis of  $Li_{6+2x}[B_{10}S_{18}]S_x$  (x = 2) with substantial  $Li_5B_7S_{13}$  and Li<sub>3</sub>BS<sub>3</sub> impurities.<sup>24</sup> Similarly, attempts to make Li<sub>5</sub>B<sub>7</sub>S<sub>13</sub>, resulted in a multiphase mixture of  $Li_{6+2x}[B_{10}S_{18}]S_x$  and  $Li_9B_{19}S_{33}$ . A more recent study of the lithium thioborate  $Li_{6+2x}[B_{10}S_{18}]S_x$  (x = 1) showed that non-stoichiometric nominal compositions with excess of B and/or S were needed for the formation of the target phase while stoichiometric nominal compositions resulted in a mixture of undesired ternary phases.<sup>26</sup> Out of the four computationally predicted phases with high conductivity,  $Li_9B_{19}S_{33}$  is expected to exhibit an impressive ionic conductivity of 80 mS/cm at 25 °C. Experimental evidence to confirm this finding has yet to be obtained. Although the crystal structure of this phase was reported three decades ago,<sup>23</sup> the syntheses of single phase samples to characterize properties remain elusive.

In this work, we describe strategies to counter the challenges encountered during the synthesis of  $Li_9B_{19}S_{33}$ . We concluded that the  $Li_9B_{19}S_{33}$  behaves as a peritectic compound, requiring an excess of  $B_2S_3$  to inhibit the formation of secondary phases such as  $Li_{6+2x}[B_{10}S_{18}]S_x$ . Hereafter, the  $Li_{6+2x}[B_{10}S_{18}]S_x$  phases, where x=1 or 2, will be referred to simply as  $LiBS_2$ . The influence of varying the amount of boron sulfide on the material's ionic conductivity was also explored. These results may inform the way for further investigations into obtaining this and other LBS phases in phase pure form and characterization of their properties.

#### **RESULTS AND DISCUSSION**

#### **Synthesis**

A high-temperature solid state approach was used to synthesize  $Li_9B_{19}S_{33}$ . In an Ar-filled glove box (< 1 ppm  $O_2$  and  $H_2O$ ), appropriate amounts of starting materials, either  $Li_2S+B+S$  or  $Li_2S+B_2S_3$ , were ground using an agate mortar and pestle to ensure a homogenous mixture. This mixture was then transferred into a carbon-coated silica ampoule. The ampoule was evacuated, sealed using a hydrogen/oxygen torch, heated to 750 °C over a period of 4h, and held for 2 h. It was then cooled to 550 °C and held for 4h before being slowly cooled to room temperature over a period of 12h. Once cooled, the ampoule was opened in the glovebox. The final product was gently separated to find crystals suitable for single crystal X-ray diffraction. The remaining crystals, and those from subsequent synthesis preparations, were crushed into a polycrystalline powder for powder X-ray diffraction (PXRD), Fourier transform infrared (FT-IR) spectroscopy, nuclear magnetic resonance (NMR) spectroscopy, UV-Vis spectroscopy, and  $Li^+$  ionic conductivity measurements.

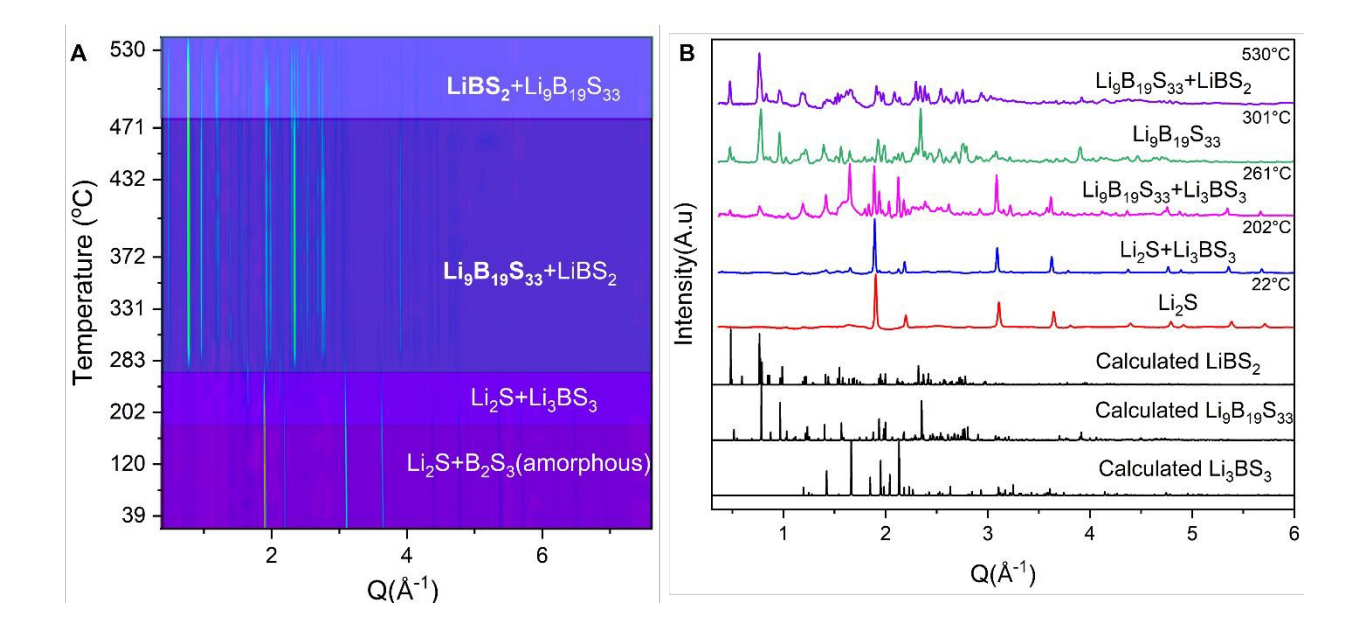


**Figure 1.** A) *In situ* powder X-ray diffraction studies on synthesis of the target phase  $Li_9B_{19}S_{33}$  showing the concurrent formation of  $LiBS_2$  over a wide temperature range. B) Selected powder patterns from in situ studies compared to calculated patterns ( $\lambda = 0.2411 \text{ Å}$ ).

Initial experiments targeting the  $\text{Li}_9\text{B}_{19}\text{S}_{33}$  phase from stoichiometric nominal compositions resulted in multiphase mixtures containing  $\text{LiBS}_2$  as major phase and  $\text{Li}_5\text{B}_7\text{S}_{13}$  as small admixture (**Table S1**). Using different reaction containers such as carbonized silica ampoules, BN crucibles, or vitreous carbon crucibles, did not change the reaction outcomes, yet some reactions of presumably  $\text{B}_2\text{S}_3$  with container or ampoule walls were observed in all cases. To overcome diffusion limitations at lower synthetic temperatures, ball-milling the reactants and pressing a pellet were attempted. Annealings of such samples at 400°C resulted in no visible reaction with container, however, such low temperature annealings led to the formation of only lithium-rich thioborate phase,  $\text{Li}_3\text{BS}_3$ . To better understand the complex synthetic processes, *in situ* PXRD was

Article. Published on 11 nóvember 2025. Downloaded on

conducted at beamline 17-BM at the Advanced Photon Source at Argonne National Laboratory (Figure 1A and 1B). From room temperature to approximately 200 °C only a single crystalline phase, Li<sub>2</sub>S, was observed. Due to the amorphous nature of B<sub>2</sub>S<sub>3</sub>, it was undetectable by PXRD. As temperature increases, a reaction between Li<sub>2</sub>S and B<sub>2</sub>S<sub>3</sub> leads to the formation of Li<sub>3</sub>BS<sub>3</sub>, which is the phase with the lowest B<sub>2</sub>S<sub>3</sub> content among the known LBS phases. The LiBS<sub>2</sub> phase forms in tandem with the target phase, Li<sub>9</sub>B<sub>19</sub>S<sub>33</sub>, starting as low as 285 °C and those two phases coexist over a wide range of temperatures. At lower temperatures (or shorter reaction times; this was a constant heating rate experiment), Li<sub>9</sub>B<sub>19</sub>S<sub>33</sub> was predominant, but with increasing time and temperature, equilibrium eventually shifts to LiBS<sub>2</sub> as the major phase.

The discrepancy between in situ and ex situ findings, particularly regarding the formation of the target phase may be attributed to variations in temperature reading accuracy, the reduced diffusion limitation due to small sample size, and, notably, the heating rates used. In situ experiments were conducted with sample size of ~20 mg and a heating rate of 20 °C/min, whereas for *ex situ* experiments the sample size was significantly larger, 300-500 mg, with a much slower heating rate of approximately 3 °C/min.

From the *in situ* PXRD experiments, we realized that obtaining phase-pure Li<sub>9</sub>B<sub>19</sub>S<sub>33</sub> from stoichiometric amounts of the reactants will be challenging, the thermodynamically stable phase (LiBS<sub>2</sub>) is likely to form in line with observations in previous studies.<sup>25</sup> It was hypothesized that the Li<sub>9</sub>B<sub>19</sub>S<sub>33</sub> phase is a peritectic, thus

Open Access Article. Published on 11 nóvember 2025. Downloaded on 14.11.2025 15:27:57

requiring excess amounts of  $B_2S_3$  for the reaction to proceed (**Figure S4**). A similar scenario was recently reported, where excess  $B_2S_3$  was needed to synthesize LiBS<sub>2</sub> without which the formation of admixtures were predominant.<sup>26</sup>

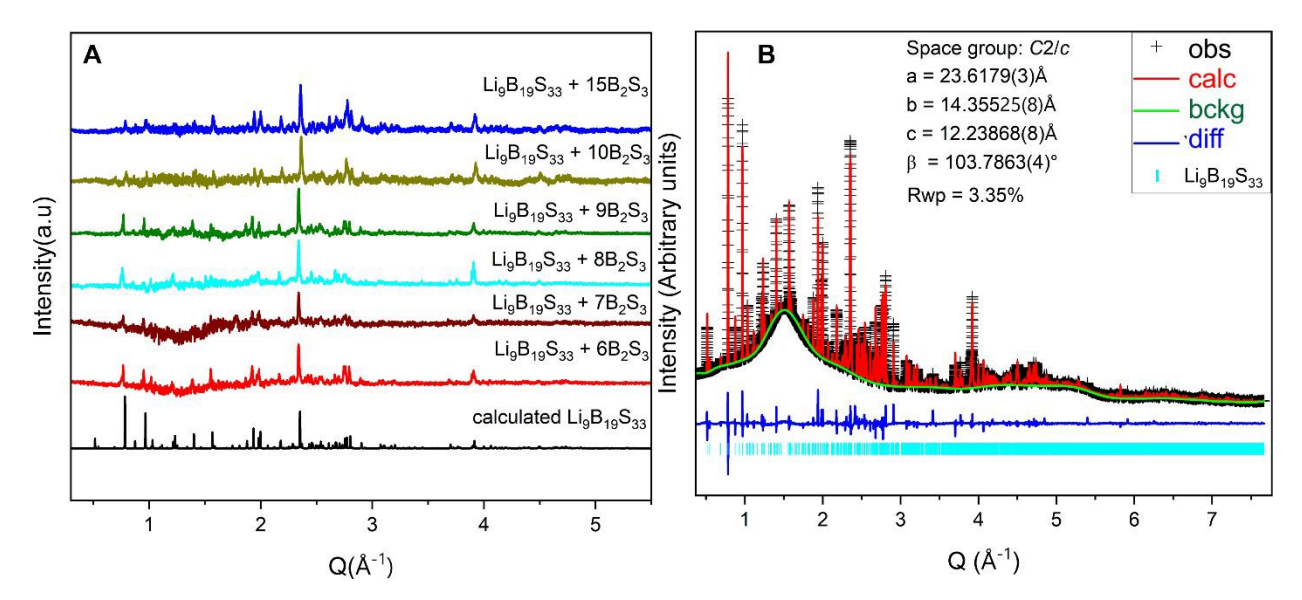


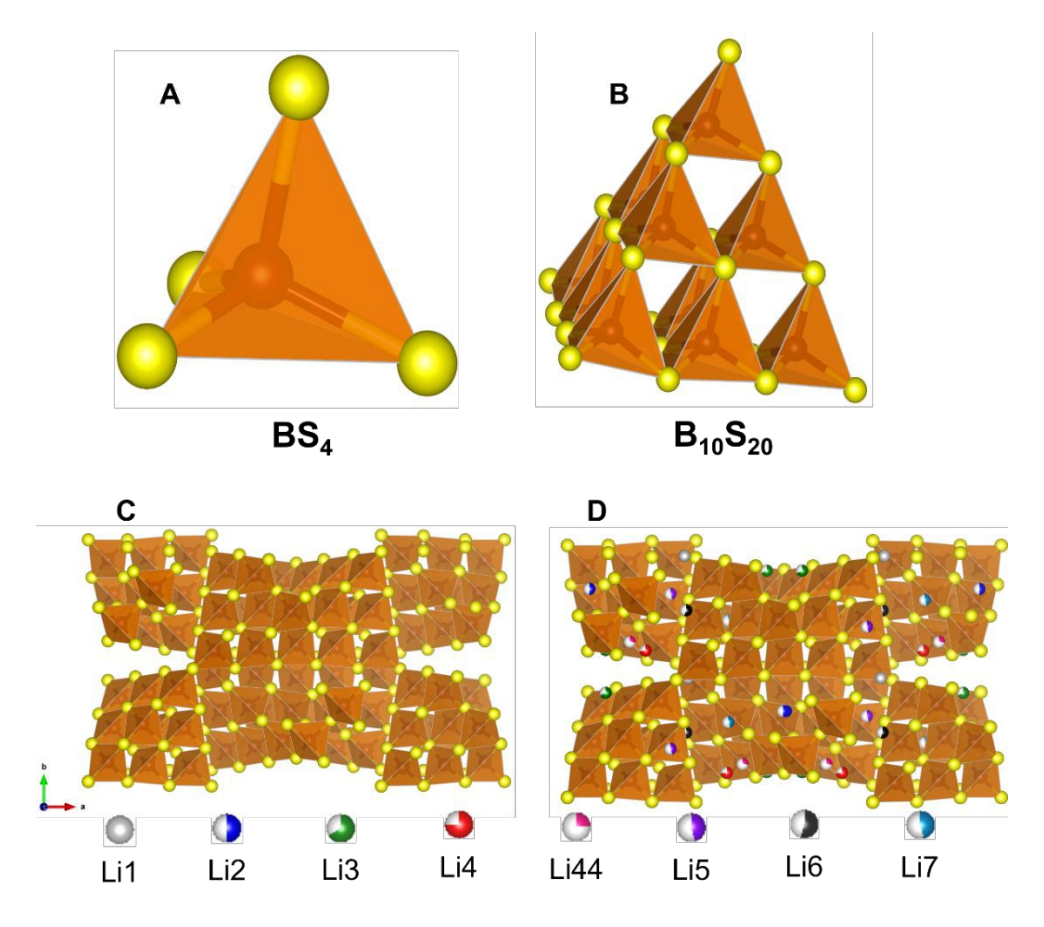
**Figure 2.** A) PXRD patterns of Li<sub>9</sub>B<sub>19</sub>S<sub>33</sub> when different excess amounts of B<sub>2</sub>S<sub>3</sub> were used for synthesis. B) Rietveld refinement of high-resolution data with wavelength  $\lambda = 0.8613$  Å.

In **Figure 2A**, PXRD patterns showed that the  $Li_9B_{19}S_{33}$  phase formed with no crystalline admixtures when 6 to 15 molar equivalent excess  $B_2S_3$  were used during the synthesis. Below this range, the formation of  $Li_9B_{19}S_{33}$  phase is challenging. The negative background around 1.1 Å<sup>-1</sup> to 1.8 Å<sup>-1</sup> is a result of subtraction from blank holders. Rietveld refinement of high-resolution room temperature synchrotron PXRD data (**Figure 2B**) confirmed the absence of secondary crystalline phases such as  $Li_2S$ ,  $Li_3BS_3$ , or  $Li_5B_7S_{13}$ , demonstrating the purity of our sample. The hump observed from 1 Å<sup>-1</sup> to 2.5

Open Access Article. Published on 11 nóvember 2025. Downloaded on 14.11.2025 15:27:57.

Å<sup>-1</sup> in **Figure 2B** is a result of some leftover B<sub>2</sub>S<sub>3</sub> because this sample was prepared with excess 15 molar equivalents of B<sub>2</sub>S<sub>3</sub> with respect to Li<sub>9</sub>B<sub>19</sub>S<sub>33</sub>. The refinement was done using a crystal structure model derived from single crystal X-ray diffraction studies. The diffraction pattern obtained can be indexed to a monoclinic unit cell with parameters a = 23.618(3) Å, b = 14.355(8) Å, c = 12.239(8) Å, and  $\beta = 103.79(4)$  Å. There are no unaccountable peaks, and the lattice parameters are close to the initially reported crystal structure by Krebs et al.23 In this way, a reasonable agreement between the experimental and calculated patterns was achieved.

#### **Crystal Structure**



Article. Published on 11 nóvember 2025. Downloaded on 14.11.2025 15:27:57

Single crystal X-ray diffraction (SCXRD) findings align with an initial report<sup>23</sup> that Li<sub>9</sub>B<sub>19</sub>S<sub>33</sub> crystallizes in the C2/c space group; however, we observed a lower unit cell volume due to differences in the experiment temperatures (173 vs 298 K). The crystal structure of Li<sub>9</sub>B<sub>19</sub>S<sub>33</sub> consists of boron tetrahedrally coordinated to sulfur, forming a super tetrahedral structure made up of corner-sharing  $B_{10}S_{20}$  units (**Figures 3B** and 3**C**). Lithium atoms are distributed over 7 Li sites located in the framework channels. The main disparity between the structure determined here and previously reported crystal structures lies in the differences in Li occupancies, as shown in Table S2. There is an additional disorder in the Li sublattices, such as the split Li site labelled Li4 and Li44 which have 73% and 27% occupancies, respectively, (Figure S3). Lithium atoms have different coordination environment in this structure. Li1, Li2, Li3, Li4, Li5, and Li6 have distorted octahedral coordination by 6 S atoms, whereas Li44 and Li7 are tetrahedrally coordinated by 4 S atoms. The majority of Li@S<sub>x</sub> polyhedra are interconnected through corner sharing. Additionally, polyhedra around Li2, Li44, and Li7 are linked via edge-sharing connections (Figure S6).

NMR and FT-IR Spectroscopy

Given that an excess of B<sub>2</sub>S<sub>3</sub> is required to drive the formation of the target phase, it is important to account for the unreacted B<sub>2</sub>S<sub>3</sub> remaining after synthesis, as it is not fully incorporated into the final product. Interestingly, it is observed that B<sub>2</sub>S<sub>3</sub> tends to segregate on the outer surface of the reaction ingot, where it reacts with the silica ampoule (Figures S10 and S11). To further investigate this behavior, we examine the coordination environments in both the target Li<sub>9</sub>B<sub>19</sub>S<sub>33</sub> compound and B<sub>2</sub>S<sub>3</sub>. In the target compound, B is coordinated in a tetrahedral geometry by sulfur atoms, whereas in B<sub>2</sub>S<sub>3</sub>, boron adopts a trigonal-planar coordination environment. This distinction suggested the use of Fourier-transform infrared (FT-IR) spectroscopy to examine the relative amounts of tetrahedral to trigonal boron in the synthesized sample.

This article is licensed under a Creative Commons Attribution-NonCommercial 3.0 Unported Licence

Open Access Article. Published on 11 nóvember 2025. Downloaded on 14.11.2025 15:27:57

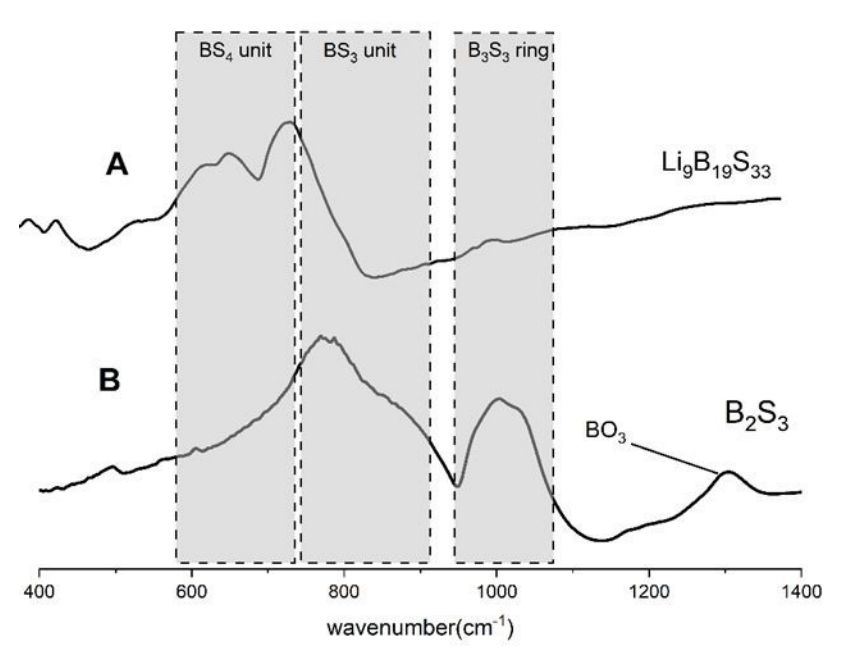


Figure 4. FT-IR spectra of A) Li<sub>9</sub>B<sub>19</sub>S<sub>33</sub> and B) B<sub>2</sub>S<sub>3</sub> samples depicting mostly BS<sub>4</sub> modes in Li<sub>9</sub>B<sub>19</sub>S<sub>33</sub> and intense BS<sub>3</sub> in the boron sulfide sample.

This article is licensed under a Creative Commons Attribution-NonCommercial 3.0 Unported Licence Article. Published on 11 nóvember 2025. Downloaded on

The sample used for this study was one synthesized with the excess amount of B<sub>2</sub>S<sub>3</sub> (8 molar equivalents). The FT-IR spectrum of B<sub>2</sub>S<sub>3</sub> (Figure 4B) reveals broad intense vibrational modes characteristic of trigonal boron environments due to its amorphous nature. Specifically, modes near >750 cm<sup>-1</sup> correspond to isolated BS<sub>3</sub> short-range order (SRO) units, while a distinct band at ~1000 cm<sup>-1</sup> is attributed to trigonal boron sites within hexagonal B<sub>3</sub>S<sub>3</sub> ring structures. Notably, vibrational modes associated with tetrahedrally coordinated boron (BS<sub>4</sub> units), which are typically expected below 700 cm<sup>-1</sup>, are absent. In contrast, the spectrum of the target compound, Li<sub>9</sub>B<sub>19</sub>S<sub>33</sub> (Figure 4A), exhibits prominent features associated with tetrahedral boron, manifested as a strong doublet centered at ~640 cm<sup>-1</sup>, ~667 cm<sup>-1</sup> and the signal ~750 cm<sup>-1</sup>. Peaks corresponding to trigonal boron environments are significantly less intense, indicating a dominant tetrahedral coordination in the final product. These assignments are based on the work of Cho et al., who investigated the FT-IR spectra of lithium thioborate polycrystals and glasses, including LiBS<sub>2</sub> and identified IR modes of BS<sub>4</sub> in 750-600 cm<sup>-1</sup> range. Both Li<sub>9</sub>B<sub>19</sub>S<sub>33</sub> and LiBS<sub>2</sub> predominantly contain tetrahedrally coordinated boron SRO units, leading to similar FT-IR spectral features.<sup>27</sup> Similar spectroscopic results were also observed for silver thioborate phases, further supporting the assignments above.<sup>28</sup> <sup>11</sup>B magic-angle spinning (MAS) solid-state NMR spectra were collected for both Li<sub>9</sub>B<sub>19</sub>S<sub>33</sub> and B<sub>2</sub>S<sub>3</sub> (used as a reference) at room temperature, Figure 5. The <sup>11</sup>B spectrum

of B<sub>2</sub>S<sub>3</sub>, Figure 5B, is dominated by a broad signal from 45 to 65 ppm, corresponding to

boron atoms in trigonal planar environments, with minor peaks corresponding to  $B_2SO$  and  $BSO_2$  SRO units which were also observed in the FT-IR spectra ~1200 cm<sup>-1</sup>.<sup>29–32</sup> Conversely, the spectrum of the  $Li_9B_{19}S_{33}$ , **Figure 5A**, predominantly features a resonance close to 0 ppm corresponding to tetrahedral  $BS_4$  SRO units, alongside minor signals corresponding to  $BS_3$ ,  $B_2SO$ ,  $BSO_2$ , and  $BO_3$  SRO units, presumably located at particle surfaces.

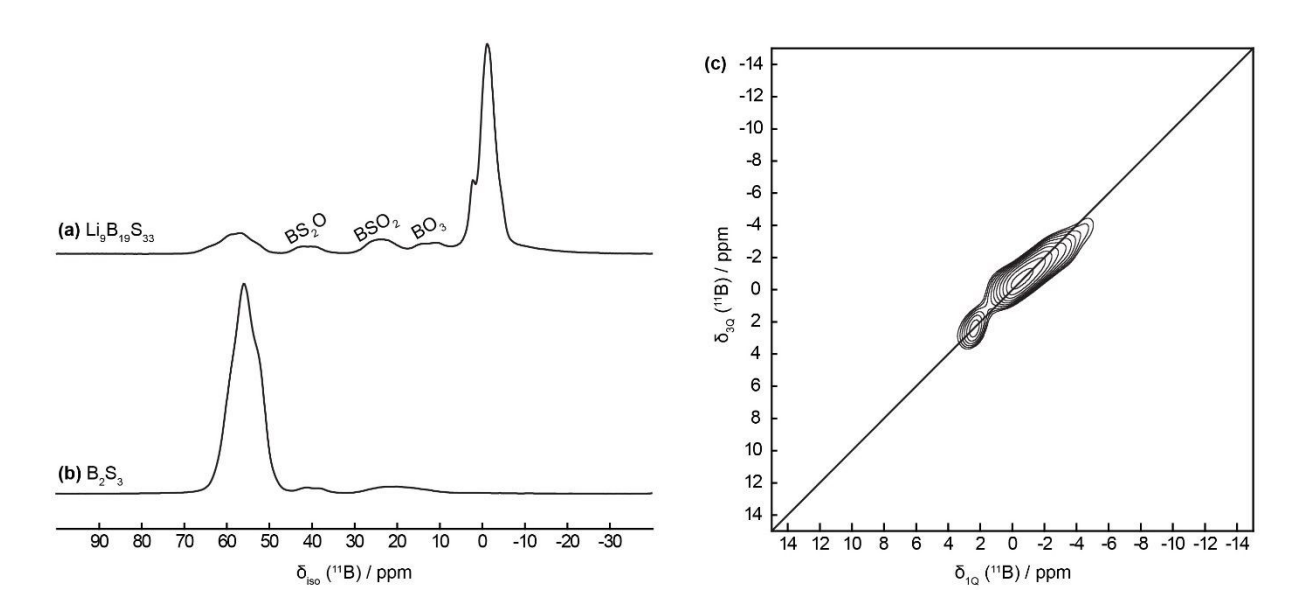


**Figure 5.** <sup>11</sup>B MAS NMR spectra of A)  $\text{Li}_9\text{B}_{19}\text{S}_{33}$  and B)  $\text{B}_2\text{S}_3$  samples. C) 2D MQMAS showing the two tetrahedral boron sites in  $\text{Li}_9\text{B}_{19}\text{S}_{33}$ .

The BS<sub>4</sub> region in the <sup>11</sup>B multiple-quantum magic-angle spinning (MQMAS) NMR spectrum (**Figure 5C**) suggests the presence of two sites, similar to what was observed for a Na<sub>3</sub>B<sub>5</sub>S<sub>9</sub> solid electrolyte.<sup>33</sup> There, two BS<sub>4</sub> fractions were identified with a 4:6 ratio, corresponding to corner and edge tetrahedral BS<sub>4</sub> species. The corner sites appear to be quite homogeneous while the edge sites appear to be broadened by a distribution of

Article. Published on 11 nóvember 2025. Downloaded on 14.11.2025 15:27:57

chemical shifts. Our NMR observations for tetrahedral B in  $\text{Li}_9\text{B}_{19}\text{S}_{33}$  (**Figure 5C**) are similar to what was observed for the  $\text{Na}_3\text{B}_5\text{S}_9$  system, suggesting a difference between the edge and corner sites in the association of lithium ions. Notably, the intensity ratio of the BS<sub>4</sub> to BS<sub>3</sub> peaks in both FT-IR and NMR spectra is approximately 80:20, indicating that despite the use of substantial molar equivalents of B<sub>2</sub>S<sub>3</sub> in addition to the stoichiometric amount required for  $\text{Li}_9\text{B}_{19}\text{S}_{33}$  synthesis, only a minimal amount of B<sub>2</sub>S<sub>3</sub> remained in the target sample after synthesis.

To determine the threshold of excess boron sulfide needed to obtain a single phase  $\text{Li}_9\text{B}_{19}\text{S}_{33}$  from PXRD, we arrayed the amounts of  $\text{B}_2\text{S}_3$ , ranging from 1 to 10 molar equivalents. It was observed that using <6 molar equivalents of  $\text{B}_2\text{S}_3$  resulted in amorphous phases or  $\text{Li}\text{BS}_2$ . Use of 6-10 molar equivalents, however, resulted in the formation of  $\text{Li}_9\text{B}_{19}\text{S}_{33}$ . <sup>11</sup>B NMR spectroscopy was used to determine the ratio of trigonal boron to tetrahedral boron in samples with 8, 9, and 10 mole equivalents of  $\text{B}_2\text{S}_3$  (**Figures S1 and S2**). A consistent decrease in the intensity of trigonal boron signal was observed when compared with nominal composition. In the sample with 8 mole equivalents of  $\text{B}_2\text{S}_3$ , the ratio of tetrahedral to trigonal boron was 85:15, indicating the losses of  $\text{B}_2\text{S}_3$  during reaction, presumably due to reaction with silica material of the ampoule.

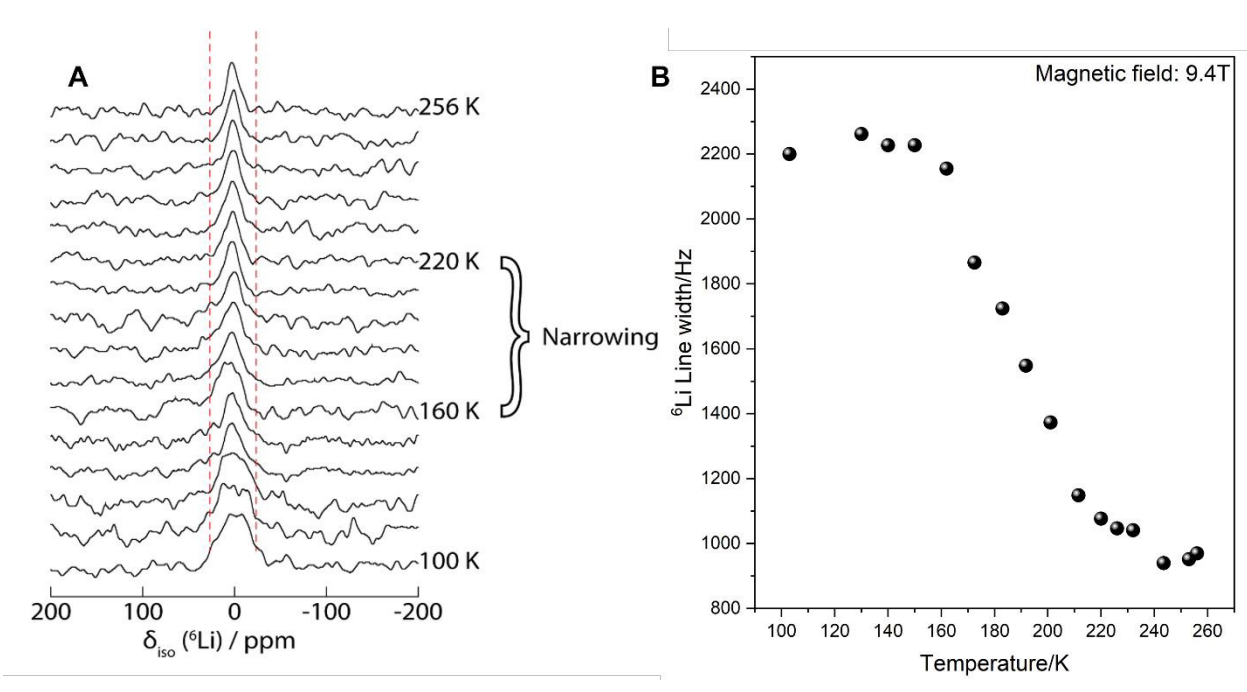


**Figure 6.** A) Variable-temperature  $^6$ Li static line width measurements for Li<sub>9</sub>B<sub>19</sub>S<sub>33</sub>. B)  $^6$ Li NMR peak width at half height as a function of temperature, highlighting the onset temperature at which linewidth narrowing occurs.

#### <sup>6</sup>Li motional line narrowing experiment

NMR spectroscopy has been widely employed to investigate microscopic lithium-ion mobility. One common approach is the Waugh-Fedin model<sup>34</sup> which enables the estimation of the activation energy ( $E_A$ ) from the motional narrowing of the static  $^6$ Li NMR line shape. Variable temperature  $^6$ Li static NMR experiments were acquired for this purpose (**Figure 6A**). The sample used in this experiment was synthesized with 15 molar equivalents of excess boron sulfide. Residual  $B_2S_3$  present after synthesis did not affect the intrinsic properties of the Li line narrowing, allowing for an accurate assessment of the material's activation energy. The spectral line shapes exhibited a transition from Gaussian to Lorentzian profiles, indicating changes in the Li-ion dynamics. With

increasing temperature, the onset of ionic motion led to the temporal averaging of anisotropic interactions. Line narrowing was first observed around 167 K and progressed until 220 K, beyond which no further narrowing occurred. Using the Waugh-Fedin model,  $^{35,36}$  the line width at half height was plotted as a function of temperature, and the extrapolated onset temperature ( $\mathcal{T}_{onset}$ ) was determined to be 162 K. The activation energy was calculated to be 0.26 eV/mol using the following relationship:

$$E_{\rm A} = 1.617 \times 10^{-3} \, \rm eV \, K^{-1} \times T_{\rm onset}$$
 (1)

This measurement is in agreement with the value of 0.23 eV measured by Krebs et al.37

#### **UV-Vis Spectroscopy**

SEs require wide bandgaps which serve to inhibit parasitic electronic conductivity and hence widen the electrochemical stability window. A study conducted by Muy *et al.* utilizing high-throughput screening of various SEs demonstrated that an increase in band gap energy correlates with a broader electrochemical stability window.<sup>38</sup> This finding highlights the necessity of selecting materials with high bandgap energies for SEs. Further investigations, including those based on DFT calculations, identified several sulfide-based SEs with bandgaps exceeding 4 eV. Notable examples include lithium thioborate such as Li<sub>3</sub>BS<sub>3</sub> and Li<sub>2</sub>B<sub>2</sub>S<sub>5</sub>, both of which exhibit bandgaps greater than 4 eV.<sup>39</sup> The large bandgaps of these materials are significant as they categorize them as electronic insulators, a crucial feature of SEs, where insulating properties help prevent

unwanted electron conduction. Sendek *et al.* employed DFT calculations to predict the electronic band gap of Li<sub>9</sub>B<sub>19</sub>S<sub>33</sub>. Their calculations estimated the bandgap to be 2.9 eV and 4.0 eV using the PBE and HSE06 exchange-correlation functionals, respectively.<sup>21</sup> While the specific nature of the energy bandgap (direct or indirect) was not explicitly stated in their work, our diffuse reflectance measured provide further insight. Direct and indirect bandgaps of 3.26(4) eV and 3.00(4) eV, respectively, were observed for Li<sub>9</sub>B<sub>19</sub>S<sub>33</sub> (Figure S5). These experimental results are consistent with the optical properties of the material, as evidenced by its nearly transparent, colorless crystals and the pale gray hue of powdered samples. This correspondence between calculated and experimentally observed bandgaps reinforces the material's potential for use in electrochemical applications requiring high electrochemical stability and low electrical conductivity.

#### Electrochemical Impedance Spectroscopy

The ionic conductivity of our target material was measured using a Novocontrol Concept 80 dielectric spectrometer. We conducted isothermal frequency scans ranging from 0.1 Hz to 7 MHz. By comparing pellets of different densities, the impact of fabrication conditions on ionic conductivity was investigated. Our findings indicated that an increase in fabrication pressure results in a linear increase in pellet density. According to Diallo *et al.*, a relative density of approximately 95 % is necessary to close any percolating pore network, which can affect the measurement of ionic conductivity. <sup>40</sup> In agreement with that

Article. Published on 11 nóvember 2025. Downloaded on 14.11.2025 15:27:57

hypothesis, a pellet of  $\text{Li}_9\text{B}_{19}\text{S}_{33}$  with a density of around 54.5 % exhibited two orders of magnitude lower ionic conductivity than that of a  $\text{Li}_9\text{B}_{19}\text{S}_{33}$  pellet with a density of 95 % (**Figure 7A**). Additionally, samples were prepared and measured with varying amounts of excess  $\text{B}_2\text{S}_3$  (**Figure 7B**). There was no significant difference in the room temperature conductivities of these samples; the conductivity at room temperature of the sample prepared with 6 molar equivalents of  $\text{B}_2\text{S}_3$  was 0.058 mS/cm, while that of the sample prepared with 8 molar equivalents was 0.052 mS/cm.

Typically, sulfide-based solid electrolytes with activation energies in this range of ~ 0.26 eV tend to exhibit ionic conductivities on the order of or exceeding 1 mS/cm. The ionic conductivity can be estimated from activation energy Arrhenius relationship

$$\sigma = \sigma_0 \exp\left(-E_a/k_B T\right) \tag{2}$$

where  $k_{\rm B}$  is the Boltzmann constant. The estimated conductivity will depend on the preexponential factor ( $\sigma_0$ ) which can be as high as ~5×10<sup>2</sup> S/cm for this class of materials.<sup>41</sup> In **Figure 7c** a range of the estimated values is shown for different values of the preexponential factor. The NMR estimated value agrees with computational predictions but is notably higher than that experimentally measured ionic conductivity. The observed discrepancies are likely due to grain boundary impedances within the pellet, as well as the presence of residual B<sub>2</sub>S<sub>3</sub>, which does not affect the NMR linewidth measurements, since NMR selectively probes Li ion dynamics through line narrowing effect.

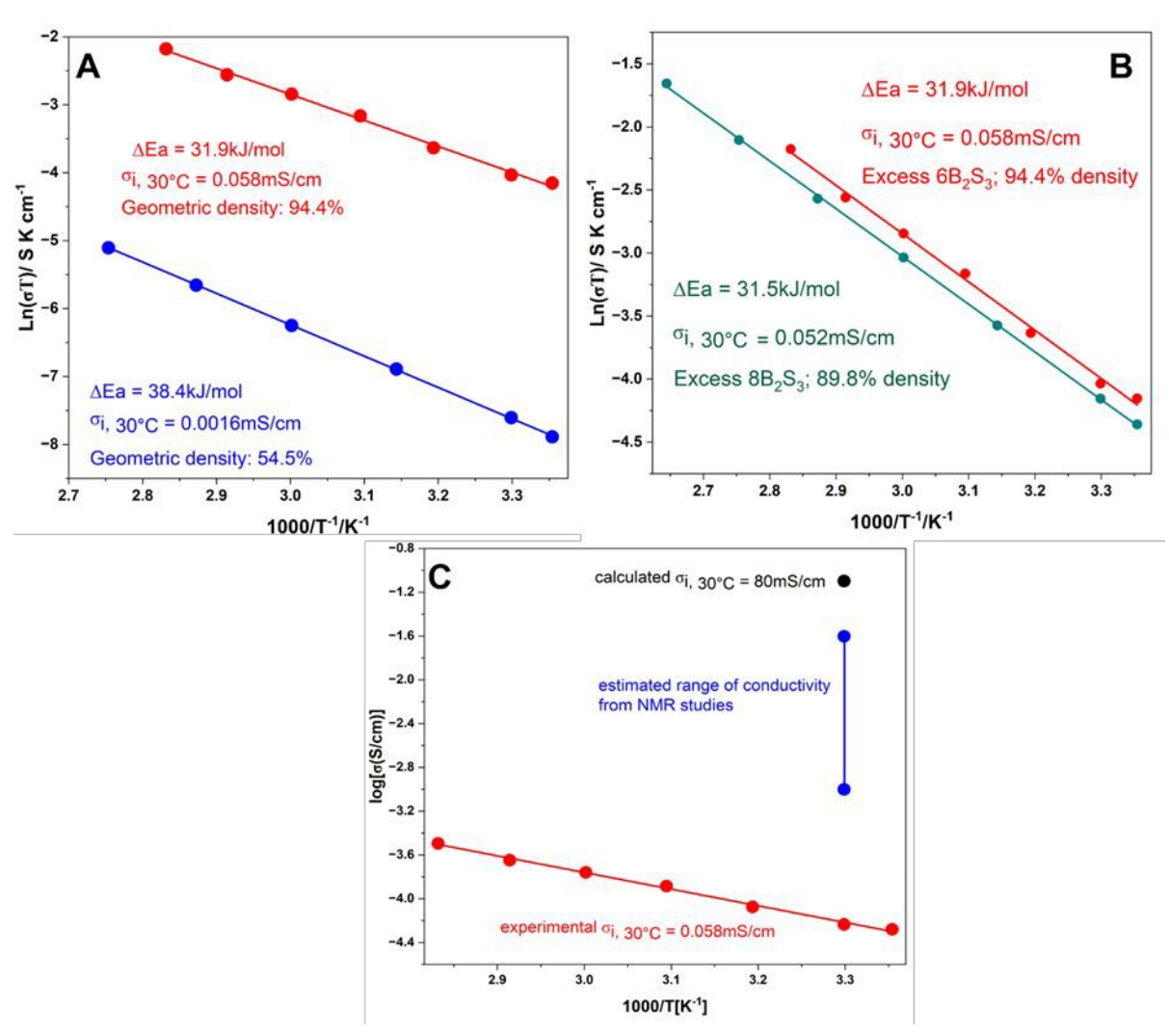


**Figure 7.** Arrhenius relationship between ionic conductivity and temperature for A)  $\text{Li}_9\text{B}_{19}\text{S}_{33}$  samples with identical nominal  $\text{B}_2\text{S}_3$  excess and with geometric density of 94.4% and 54.4% B)  $\text{Li}_9\text{B}_{19}\text{S}_{33}$  prepared with 6 and 8 equivalents of  $\text{B}_2\text{S}_3$ . C) Comparing conductivity of this work against predicted conductivity using DFT calculations in Sendek et al. and conductivity from NMR linewidth motional narrowing.

These discrepancies are not uncommon and are typically associated with the length scales of the different measurements. For instance, pulsed field gradient (PFG) NMR experiments that do probe long-range diffusion have been shown to agree relatively well with EIS for Li<sub>7</sub>SiPS<sub>8</sub>.<sup>42</sup> Relaxation characteristics and line narrowing, however, are

primarily driven by short-range dynamics such as the hopping of a Li ion between two adjacent crystallographic positions. Examples include superionic glasses  $(AgI)_x(Ag_2O\cdot 2B_2O_3)_{1-x}^{43}$  and  $Li_{4-2x}Mg_xP_2S_6$ . Additionally, Borsa *et al.* found that the preexponential factor derived from NMR measurement in Li<sub>2</sub>S-SiS<sub>2</sub> glasses was higher than that obtained from conductivity measurement by an order of magnitude.<sup>44</sup> Svare et al. reported that such discrepancies are more pronounced in disordered materials, such as the inorganic glasses, than in ordered systems such as that reported here. 45 This behavior is often attributed to the reduced average number of available hopping sites in ordered structures. Additionally, the presence of oxide impurities, as identified by FT-IR and <sup>11</sup>B NMR spectroscopy, may contribute to the observed decrease in ionic conductivity. Such impurities can disrupt the continuous sulfide framework and introduce insulating phases, thereby hindering lithium-ion migration within the structure.<sup>46</sup>

#### CONCLUSION

Crystalline lithium thioborates, while cost-effective and low mass density, have been underexplored as SEs. It was predicted that four of these phases are likely to exhibit Li<sup>+</sup> ionic conductivities much higher than 1 mS/cm, with Li<sub>9</sub>B<sub>19</sub>S<sub>33</sub> having the highest anticipated ionic conductivity. Challenges in obtaining a phase-pure version of this material prevented experimental validation. In this study, we successfully synthesized this elusive phase by optimizing the reaction conditions, aided by *in situ* powder X-ray diffraction studies. We confirmed the formation of this crystalline phase using FT-IR

spectroscopy and <sup>11</sup>B NMR techniques. We discovered that the phase is a peritectic, requiring excess boron sulfide for its formation, which resulted in residual amorphous boron sulfide within the final product. EIS measurements yielded activation energies ranging from 0.32 eV to 0.40 eV, significantly higher than that measured using <sup>6</sup>Li NMR spectroscopy (0.26 eV). Although such discrepancies are not uncommon due to the differing length scales probed by these measurement techniques, the observed variation in ionic conductivity is notably large. This suggests that the material's performance as an ion conductor could be further enhanced through additional synthetic modifications aimed at removing residual boron sulfide.

#### **Supporting Information**

This article is licensed under a Creative Commons Attribution-NonCommercial 3.0 Unported Licence

Article. Published on 11 nóvember 2025. Downloaded on 14.11.2025 15:27:57

Supporting Information is available for free and includes a description of the synthetic and characterization experimental procedures, as well as additional tables and figures related diffuse reflectance spectroscopy, crystallographic data, differential scanning calorimetry (DSC) and a schematic phase diagram of Li<sub>9</sub>B<sub>19</sub>S<sub>33</sub>. It also features FT-IR and NMR spectra of Li<sub>9</sub>B<sub>19</sub>S<sub>33</sub> samples synthesized with varying amounts of excess B<sub>2</sub>S<sub>3</sub>, along with a comparison of the unit cells of our synthesized Li<sub>9</sub>B<sub>19</sub>S<sub>33</sub> to those reported in the literature, highlighting the lithium sites and their occupancies.

#### AUTHOR INFORMATION

#### **Corresponding Author**

Dr. Kirill Kovnir, kovnir@iastate.edu, Steve W. Martin swmartin@iastate.edu

Article. Published on 11 nóvember 2025. Downloaded on

#### **Author Contributions**

The manuscript was written through contributions of all authors.

#### **Funding Sources**

This research was supported by the National Science Foundation ENG/CBET EAGER grant # 2234046. The FTIR spectrometer used in this study was supported by NSF MRI grant 2117445. Use of the Advanced Photon Source was supported by U.S. Department of Energy, Office of Basic Energy Sciences, under Contract No. DE-AC02-06CH11357. Part of the research described in this paper was performed at the Canadian Light Source, a national research facility of the University of Saskatchewan, which is supported by the Canada Foundation for Innovation (CFI), the Natural Sciences and Engineering Research Council (NSERC), the Canadian Institutes of Health Research (CIHR), the Government of Saskatchewan, and the University of Saskatchewan. Solid-state NMR measurements were supported by the U.S. Department of Energy, Office of Science, Basic Energy Sciences, Materials Science and Engineering Division. The Ames National Laboratory is operated for the U.S. DOE by Iowa State University under Contract No. DE-AC02-07CH11358.

#### Acknowledgements

The authors would like to thank Prof. J.V. Zaikina (ISU) for access to the SPS and UV-vis spectrometer; Dr. W. Xu, for help with conducting *in situ* PXRD at beamline 17-BM at

APS-ANL, and Dr. Adam Leontowich at the Canadian Light Source, BXDS beamline for help with collecting the high-resolution PXRD used for Rietveld refinement.

#### REFERENCES

- (1) Banerjee, A.; Wang, X.; Fang, C.; Wu, E. A.; Meng, Y. S. Interfaces and Interphases in All-Solid-State Batteries with Inorganic Solid Electrolytes. *Chem. Rev.* 2020, 120 (14), 6878–6933. https://doi.org/10.1021/acs.chemrev.0c00101.
- (2) Croce, F.; Appetecchi, G. B.; Persi, L.; Scrosati, B. Nanocomposite Polymer Electrolytes for Lithium Batteries. *Nature* **1998**, *394* (6692), 456–458. https://doi.org/10.1038/28818.
- (3) Zhou, D.; Shanmukaraj, D.; Tkacheva, A.; Armand, M.; Wang, G. Polymer Electrolytes for Lithium-Based Batteries: Advances and Prospects. *Chem* 2019, *5* (9), 2326–2352. https://doi.org/10.1016/j.chempr.2019.05.009.
- (4) Yao, X.; Huang, B.; Yin, J.; Peng, G.; Huang, Z.; Gao, C.; Liu, D.; Xu, X. All-Solid-State Lithium Batteries with Inorganic Solid Electrolytes: Review of Fundamental Science\*. *Chin. Phys. B* 2015, *25* (1), 018802. https://doi.org/10.1088/1674-1056/25/1/018802.
- (5) Matsuo, M.; Orimo, S. Lithium Fast-Ionic Conduction in Complex Hydrides: Review and Prospects. Adv. Energy Mater. 2011, 1 (2), 161–172. https://doi.org/10.1002/aenm.201000012.
- (6) Li, X.; Liang, J.; Chen, N.; Luo, J.; Adair, K. R.; Wang, C.; Banis, M. N.; Sham, T.-K.; Zhang, L.; Zhao, S.; Lu, S.; Huang, H.; Li, R.; Sun, X. Water-Mediated Synthesis of a Superionic Halide Solid Electrolyte. *Angew. Chem.* 2019, *131* (46), 16579–16584. https://doi.org/10.1002/ange.201909805.
- (7) Li, X.; Liang, J.; Luo, J.; Banis, M. N.; Wang, C.; Li, W.; Deng, S.; Yu, C.; Zhao, F.; Hu, Y.; Sham, T.-K.; Zhang, L.; Zhao, S.; Lu, S.; Huang, H.; Li, R.; R. Adair, K.; Sun, X. Air-Stable Li 3 InCl 6 Electrolyte with High Voltage Compatibility for All-

Article. Published on 11 nóvember 2025. Downloaded on 14.11.2025 15:27:57

- Solid-State Batteries. *Energy Environ. Sci.* **2019**, *12* (9), 2665–2671. https://doi.org/10.1039/C9EE02311A.
- (8) Tatsumisago, M.; Hayashi, A. Sulfide Glass-Ceramic Electrolytes for All-Solid-State Lithium and Sodium Batteries. *Int. J. Appl. Glass Sci.* 2014, 5 (3), 226–235. https://doi.org/10.1111/ijag.12084.
- (9) Kato, Y.; Hori, S.; Saito, T.; Suzuki, K.; Hirayama, M.; Mitsui, A.; Yonemura, M.; Iba, H.; Kanno, R. High-Power All-Solid-State Batteries Using Sulfide Superionic Conductors. *Nat. Energy* 2016, 1 (4), 1–7. https://doi.org/10.1038/nenergy.2016.30.
- (10) Zhao, Q.; Stalin, S.; Zhao, C.-Z.; Archer, L. A. Designing Solid-State Electrolytes for Safe, Energy-Dense Batteries. *Nat. Rev. Mater.* 2020, 5 (3), 229–252. https://doi.org/10.1038/s41578-019-0165-5.
- (11) Tan, D. H. S.; Banerjee, A.; Chen, Z.; Meng, Y. S. From Nanoscale Interface Characterization to Sustainable Energy Storage Using All-Solid-State Batteries. *Nat. Nanotechnol.* **2020**, *15* (3), 170–180. https://doi.org/10.1038/s41565-020-0657-x.
- (12) Gao, Z.; Sun, H.; Fu, L.; Ye, F.; Zhang, Y.; Luo, W.; Huang, Y. Promises, Challenges, and Recent Progress of Inorganic Solid-State Electrolytes for All-Solid-State Lithium Batteries. *Adv. Mater.* 2018, *30* (17), 1705702. https://doi.org/10.1002/adma.201705702.
- (13) Kanno, R.; Murayama, M. Lithium Ionic Conductor Thio-LISICON: The Li<sub>2</sub>S-GeS<sub>2</sub>-P<sub>2</sub>S<sub>5</sub> System. *J. Electrochem. Soc.* 2001, 148 (7), A742. https://doi.org/10.1149/1.1379028.
- (14) Famprikis, T.; Canepa, P.; Dawson, J. A.; Islam, M. S.; Masquelier, C. Fundamentals of Inorganic Solid-State Electrolytes for Batteries. *Nat. Mater.* 2019, 18 (12), 1278–1291. https://doi.org/10.1038/s41563-019-0431-3.
- (15) Han, A.; Tian, R.; Fang, L.; Wan, F.; Hu, X.; Zhao, Z.; Tu, F.; Song, D.; Zhang, X.; Yang, Y. A Low-Cost Liquid-Phase Method of Synthesizing High-Performance

- Li<sub>6</sub>PS<sub>5</sub>Cl Solid-Electrolyte. *ACS Appl. Mater. Interfaces* **2022**, *14* (27), 30824–30838. https://doi.org/10.1021/acsami.2c06075.
- (16) Wang, S.; Zhang, Y.; Zhang, X.; Liu, T.; Lin, Y.-H.; Shen, Y.; Li, L.; Nan, C.-W. High-Conductivity Argyrodite Li<sub>6</sub>PS<sub>5</sub>Cl Solid Electrolytes Prepared via Optimized Sintering Processes for All-Solid-State Lithium–Sulfur Batteries. *ACS Appl. Mater. Interfaces* 2018, 10 (49), 42279–42285. https://doi.org/10.1021/acsami.8b15121.
- (17) Busche, M. R.; Weber, D. A.; Schneider, Y.; Dietrich, C.; Wenzel, S.; Leichtweiss, T.; Schröder, D.; Zhang, W.; Weigand, H.; Walter, D.; Sedlmaier, S. J.; Houtarde, D.; Nazar, L. F.; Janek, J. In Situ Monitoring of Fast Li-lon Conductor Li<sub>7</sub>P<sub>3</sub>S<sub>11</sub> Crystallization Inside a Hot-Press Setup. *Chem. Mater.* 2016, *28* (17), 6152–6165. https://doi.org/10.1021/acs.chemmater.6b02163.
- (18) Bron, P.; Dehnen, S.; Roling, B. Li<sub>10</sub>Si<sub>0.3</sub>Sn<sub>0.7</sub>P<sub>2</sub>S<sub>12</sub> A Low-Cost and Low-Grain-Boundary-Resistance Lithium Superionic Conductor. *J. Power Sources* **2016**, *329*, 530–535. https://doi.org/10.1016/j.jpowsour.2016.08.115.
- (19) Kamaya, N.; Homma, K.; Yamakawa, Y.; Hirayama, M.; Kanno, R.; Yonemura, M.; Kamiyama, T.; Kato, Y.; Hama, S.; Kawamoto, K.; Mitsui, A. A Lithium Superionic Conductor. *Nat. Mater.* **2011**, *10* (9), 682–686. https://doi.org/10.1038/nmat3066.
- (20) Huang, Y.; Shao, B.; Han, F. Interfacial Challenges in All-Solid-State Lithium Batteries. *Curr. Opin. Electrochem.* 2022, *33*, 100933. https://doi.org/10.1016/j.coelec.2021.100933.
- (21) Sendek, A. D.; Antoniuk, E. R.; Cubuk, E. D.; Ransom, B.; Francisco, B. E.; Buettner-Garrett, J.; Cui, Y.; Reed, E. J. Combining Superionic Conduction and Favorable Decomposition Products in the Crystalline Lithium–Boron–Sulfur System: A New Mechanism for Stabilizing Solid Li-Ion Electrolytes. *ACS Appl. Mater. Interfaces* 2020, 12 (34), 37957–37966. https://doi.org/10.1021/acsami.9b19091.

Article. Published on 11 nóvember 2025. Downloaded on 14.11.2025 15:27:57

- (22) Zhu, X.; Zhang, Z.; Chen, L.; Li, H.; Wu, F. Progress in Lithium Thioborate Superionic Conductors. *J. Mater. Res.* 2022, 37 (19), 3269–3282. https://doi.org/10.1557/s43578-022-00592-4.
- (23) Hiltmann, F.; Zum Hebel, P.; Hammerschmidt, A.; Krebs, B. Li<sub>5</sub>B<sub>7</sub>S<sub>13</sub> und Li<sub>9</sub>B<sub>19</sub>S<sub>33</sub>: Zwei Lithiumthioborate mit neuen hochpolymeren Anionengerüsten. *Z. Anorg. Allg. Chem.* **1993**, *619* (2), 293–302. https://doi.org/10.1002/zaac.19936190212.
- (24) Kaup, K.; Assoud, A.; Liu, J.; Nazar, L. F. Fast Li-Ion Conductivity in Superadamantanoid Lithium Thioborate Halides. *Angew. Chem. Int. Ed.* **2021**, *60* (13), 6975–6980. https://doi.org/10.1002/anie.202013339.
- (25) Kaup, K.; Bishop, K.; Assoud, A.; Liu, J.; Nazar, L. F. Fast Ion-Conducting
  Thioboracite with a Perovskite Topology and Argyrodite-like Lithium Substructure. *J. Am. Chem. Soc.* **2021**, *143* (18), 6952–6961.

  https://doi.org/10.1021/jacs.1c00941.
- (26) Ma, Y.; Wan, J.; Xu, X.; Sendek, A. D.; Holmes, S. E.; Ransom, B.; Jiang, Z.; Zhang, P.; Xiao, X.; Zhang, W.; Xu, R.; Liu, F.; Ye, Y.; Kaeli, E.; Reed, E. J.; Chueh, W. C.; Cui, Y. Experimental Discovery of a Fast and Stable Lithium Thioborate Solid Electrolyte, Li<sub>6+2x</sub>[B<sub>10</sub>S<sub>18</sub>]S<sub>x</sub> (x ≈ 1). ACS Energy Lett. 2023, 8 (6), 2762–2771. https://doi.org/10.1021/acsenergylett.3c00560.
- (27) Cho, J.; Martin, S. W. Infrared Spectra of Lithium Thioborate Glasses and Polycrystals. *J. Non-Cryst. Solids* **1994**, *170* (2), 182–189. https://doi.org/10.1016/0022-3093(94)90045-0.
- (28) Burns, A. E.; Royle, M.; Martin, S. W. Infrared Spectroscopy of Agl Doped Ag<sub>2</sub>S+B<sub>2</sub>S<sub>3</sub> Fast Ion Conducting Thioborate Glasses. *J. Non-Cryst. Solids* **2000**, *262* (1), 252–257. https://doi.org/10.1016/S0022-3093(99)00652-3.
- (29) Hwang, S.-J.; Fernandez, C.; Amoureux, J. P.; Cho, J.; Martin, S. W.; Pruski, M. Quantitative Study of the Short Range Order in B<sub>2</sub>O<sub>3</sub> and B<sub>2</sub>S<sub>3</sub> by MAS and Two-Dimensional Triple-Quantum MAS <sup>11</sup>B NMR. *Solid State Nucl. Magn. Reson.* **1997**, 8 (2), 109–121. https://doi.org/10.1016/S0926-2040(96)01280-5.

- (30) Curtis, B.; Francis, C.; Kmiec, S.; Martin, S. W. Investigation of the Short Range Order Structures in Sodium Thioborosilicate Mixed Glass Former Glasses. *J. Non-Cryst. Solids* 2019, *521*, 119456. https://doi.org/10.1016/j.jnoncrysol.2019.05.032.
- (31) Hwang, S.-J.; Fernandez, C.; Amoureux, J. P.; Han, J.-W.; Cho, J.; Martin, S. W.; Pruski, M. Structural Study of xNa<sub>2</sub>S+(1-x)B<sub>2</sub>S<sub>3</sub> Glasses and Polycrystals by Multiple-Quantum MAS NMR of <sup>11</sup>B and <sup>23</sup>Na. *J. Am. Chem. Soc.* **1998**, *120* (29), 7337–7346. https://doi.org/10.1021/ja9800481.
- (32) Martin, S. W.; Christensen, R.; Olson, G.; Kieffer, J.; Wang, W. New Interpretation of Na<sup>+</sup>-Ion Conduction in and the Structures and Properties of Sodium Borosilicate Mixed Glass Former Glasses. *J. Phys. Chem. C* 2019, *123* (10), 5853–5870. https://doi.org/10.1021/acs.jpcc.8b11735.
- (33) Zhou, L.; Bazak, J. D.; Singh, B.; Li, C.; Assoud, A.; Washton, N. M.; Murugesan, V.; Nazar, L. F. A New Sodium Thioborate Fast Ion Conductor: Na<sub>3</sub>B<sub>5</sub>S<sub>9</sub>. *Angew. Chem. Int. Ed. n/a* (n/a), e202300404. https://doi.org/10.1002/anie.202300404.
- (34) Waugh, J.; Fedin, E. Determination of Hindered-Rotation Barriers in Solids. *Sov. Phys.-SOLID STATE* **1963**, *4* (8), 1633–1636.
- (35) Kaib, T.; Haddadpour, S.; Kapitein, M.; Bron, P.; Schröder, C.; Eckert, H.; Roling, B.; Dehnen, S. New Lithium Chalcogenidotetrelates, LiChT: Synthesis and Characterization of the Li<sup>+</sup>-Conducting Tetralithium Ortho-Sulfidostannate Li<sub>4</sub>SnS<sub>4</sub>. *Chem. Mater.* 2012, *24* (11), 2211–2219. https://doi.org/10.1021/cm3011315.
- (36) Neuberger, S.; Mathew, N.; Clement Adediwura, S.; Günne, J. S. auf der. Influence of Mg on the Li Ion Mobility in Li<sub>4-2x</sub>Mg<sub>x</sub>P<sub>2</sub>S<sub>6</sub>. *Dalton Trans.* **2023**, *52* (45), 16894–16902. https://doi.org/10.1039/D3DT02624H.
- (37) Bertermann, R.; Müller-Warmuth, W.; Jansen, C.; Hiltmann, F.; Krebs, B. NMR Studies of the Lithium Dynamics in Two Thioborate Superionic Conductors:  $\text{Li}_9\text{B}_{19}\text{S}_{33}$  and  $\text{Li}_{4-2x}\text{Sr}_{2+x}\text{B}_{10}\text{S}_{19}$  (x≈0.27). *Solid State Ion.* **1999**, *117* (3), 245–255. https://doi.org/10.1016/S0167-2738(98)00407-X.

Article. Published on 11 nóvember 2025. Downloaded on 14.11.2025 15:27:57

- (38) Muy, S.; Voss, J.; Schlem, R.; Koerver, R.; Sedlmaier, S. J.; Maglia, F.; Lamp, P.; Zeier, W. G.; Shao-Horn, Y. High-Throughput Screening of Solid-State Li-Ion Conductors Using Lattice-Dynamics Descriptors. *iScience* 2019, *16*, 270–282. https://doi.org/10.1016/j.isci.2019.05.036.
- (39) Park, H.; Yu, S.; Siegel, D. J. Predicting Charge Transfer Stability between Sulfide Solid Electrolytes and Li Metal Anodes. *ACS Energy Lett.* **2021**, *6* (1), 150–157. https://doi.org/10.1021/acsenergylett.0c02372.
- (40) Diallo, M. S.; Shi, T.; Zhang, Y.; Peng, X.; Shozib, I.; Wang, Y.; Miara, L. J.; Scott, M. C.; Tu, Q. H.; Ceder, G. Effect of Solid-Electrolyte Pellet Density on Failure of Solid-State Batteries. *Nat. Commun.* 2024, 15 (1), 858. https://doi.org/10.1038/s41467-024-45030-7.
- (41) Muy, S.; Bachman, J. C.; Chang, H.-H.; Giordano, L.; Maglia, F.; Lupart, S.; Lamp, P.; Zeier, W. G.; Shao-Horn, Y. Lithium Conductivity and Meyer-Neldel Rule in Li<sub>3</sub>PO<sub>4</sub>–Li<sub>3</sub>VO<sub>4</sub>–Li<sub>4</sub>GeO<sub>4</sub> Lithium Superionic Conductors. *Chem. Mater.* **2018**, *30* (16), 5573–5582. https://doi.org/10.1021/acs.chemmater.8b01504.
- (42) Harm, S.; Hatz, A.-K.; Moudrakovski, I.; Eger, R.; Kuhn, A.; Hoch, C.; Lotsch, B. V. Lesson Learned from NMR: Characterization and Ionic Conductivity of LGPS-like Li<sub>7</sub>SiPS<sub>8</sub>. *Chem. Mater.* **2019**, *31* (4), 1280–1288. https://doi.org/10.1021/acs.chemmater.8b04051.
- (43) Martin, S. W.; Bischof, H. J.; Mali, M.; Roos, J.; Brinkmann, D. 109Ag NMR Investigations of the Superionic Glasses (AgI)<sub>x</sub>·(Ag<sub>2</sub>O·2B<sub>2</sub>O<sub>3</sub>)<sub>1-x</sub>. Solid State Ion. 1986, 18–19, 421–425. https://doi.org/10.1016/0167-2738(86)90153-0.
- (44) Borsa, F.; Torgeson, D. R.; Martin, S. W.; Patel, H. K. Relaxation and Fluctuations in Glassy Fast-Ion Conductors: Wide-Frequency-Range NMR and Conductivity Measurements. *Phys. Rev. B* 1992, *46* (2), 795–800. https://doi.org/10.1103/PhysRevB.46.795.
- (45) Svare, I.; Borsa, F.; Torgeson, D. R.; Martin, S. W. Correlation Functions for Ionic Motion from NMR Relaxation and Electrical Conductivity in the Glassy Fast-Ion

- Conductor ( $Li_2S$ )<sub>0.56</sub>( $SiS_2$ )<sub>0.44</sub>. *Phys. Rev. B* **1993**, *48* (13), 9336–9344. https://doi.org/10.1103/PhysRevB.48.9336.
- (46) Mi, C.; Hall, S. R. Preparation and Degradation of High Air Stability Sulfide Solid Electrolyte 75Li<sub>2</sub>S·25P<sub>2</sub>S<sub>5</sub> Glass-Ceramic. *Solid State Ion.* **2023**, *389*, 116106. https://doi.org/10.1016/j.ssi.2022.116106.

## Come for predictions, stay for complexity: Synthesis and experimental probing of ionic conductivity in Li<sub>9</sub>B<sub>19</sub>S<sub>33</sub>

Richeal A. Oppong<sup>1,2</sup>, Scott A. Southern<sup>3</sup>, Chris Martin<sup>2</sup>, Isabella Freebairn<sup>1</sup>, Arka Sarkar<sup>1,4</sup>, Yao Abusa<sup>1</sup>, Gayatri Viswanathan<sup>1,4</sup>, Frédéric A. Perras<sup>1,3</sup>, Steve W. Martin<sup>2,\*</sup>, Kirill Kovnir<sup>1,4\*</sup>

### **Data Availability Statement**

- ➤ The data supporting this article have been included as part of the Supplementary Information.
- ➤ Crystallographic data for Li<sub>9</sub>B<sub>19</sub>S<sub>33</sub> has been deposited at the joint CCDC/FIZ Karlsruhe online deposition service: <a href="https://www.ccdc.cam.ac.uk/structures/">https://www.ccdc.cam.ac.uk/structures/</a>? and can be retrieved by quoting the deposition number CSD- 2475362.